SCIENCE CHINA Materials

Mechanical and corrosion properties of partially degradable bone screws made of pure iron and stainless steel 316L by friction welding

Nasution Ahmad Kafrawi, Ulum Mokhamad Fakhrul, Abdul Kadir Mohammed Rafiq and Hermawan Hendra

Citation: SCIENCE CHINA Materials ; doi: 10.1007/s40843-017-9057-3

View online: http://engine.scichina.com/doi/10.1007/s40843-017-9057-3

Published by the Science China Press

Mechanical and corrosion properties of partially degradable bone screws made of pure iron and stainless steel 316L by friction welding

Journal:	*SCIENCE CHINA Materials*
Manuscript ID	SCMs-2017-0060.R1
Manuscript Type:	Article
Date Submitted by the Author:	18-May-2017
Complete List of Authors:	Nasution, Ahmad Kafrawi; Universitas Muhammadiyah Riau, Mechanical Engineering Ulum, Mokhamad Fakhrul; Institut Pertanian Bogor, Veterinary Medicine Abdul Kadir, Mohammed Rafiq; Universiti Teknologi Malaysia, Biomedical Engineering Hermawan, Hendra; Laval University, Materials Engineering
Keywords:	biodegradable metal, bone screw, friction welding, in vivo, iron, stainless steel
Speciality:	biodegradable metal

Mechanical and corrosion properties of partially degradable bone screws made of pure iron and stainless steel 316L by friction welding

Ahmad Kafrawi Nasution[1], Mohammad Fakhrul Ulum[2], Mohammed Rafiq Abdul Kadir[3], Hendra Hermawan[4*]

[1]Dept. of Mechanical Engineering, Faculty of Engineering, Muhammadiyah University of Riau, Pekanbaru 28122, Indonesia

[2]Faculty of Veterinary Medicine, Bogor Agricultural University, Bogor 16680, Indonesia

[3]Faculty of Biosciences and Medical Engineering, Universiti Teknologi Malaysia, Johor Bahru 81310, Malaysia

[4]Dept. of Mining, Metallurgical and Materials Engineering & CHU de Québec Research Center, Laval University, Quebec City G1V 0A6, Canada

*Corresponding author (e-mail: hendra.hermawan@gmn.ulaval.ca)

ABSTRACT: This paper reports a series of in vitro, ex vivo and in vivo mechanical and corrosion studies of pin and screw prototype made of friction welded pure iron and 316L type stainless steel aiming to evaluate the applicability of the partially removable bone screws. Results showed that the pin possesses bending, tensile and torsional strengths of 1.7 GPa, 660 MPa and 0.34 MPa, respectively. The pin degraded at an average weight loss rate of 17.15 x 10^{-5} g/cm^2.day and released Fe ions at an average concentration of 2.38 ppm. Plastic deformation induced by torsion increased the corrosion rate of the pin from 0.0014 to 0.0137 mm/year. The maximum pull-out load of the screw prototypes was 3800 N with a calculated failure strength by shear load equal to 22.2 kN which is higher than the strength of the cortical bone. Detailed analysis of the rat's blood cells during 60 days of the pin implantation indicated a normal response with low neutrophils/lymphocytes ratio of 0.3-0.5. Iron ion concentration in the rat's blood slightly increased from 55 to 61 ppm without affecting the tissue recovering and healing phase. Histological evaluation confirmed the presence of macrophage cells as a normal response to the released iron particles around the iron section of the pin.

Keywords: biodegradable metal, bone screw, friction welding, in vivo, iron, stainless steel

INTRODUCTION

Metallic implants used for fixing a fractured bone such as screws are usually removed after the fractured bone is healed and united. This procedure is normally done within a time span of one to two years to avoid bone refracture [1, 2]. However, the necessity of this procedure is still debatable [3]. Although it is recommended to remove the screws when tissue rejection complications occur, e.g. an allergic reaction [3, 4], the screws may still need to remain attached to the bones for functional reasons, e.g. avoiding bone refracture [5, 6]. Beyond this debate, a partially removable bone screw is an interesting potential solution to address the controversy. The concept is that a half of the screw can be removed after the necessary healing period to avoid allergic reactions while the other half stays intact within the bone to avoid refracture. Thereafter, the intact part is expected to degrade progressively. At the end of the bone healing period, there will be no implant left behind while the bone returns to its normal biomechanical condition.

The above-mentioned concept needs a joint usage of inert materials such as type 316L stainless steel (SS316L) with biodegradable/bioabsorbable materials. Biodegradable orthopaedic implants have been in clinical use since a decade ago where biodegradable polymers such as the poly(lactic acid) and poly(caprolactone) families have been used as the materials [7]. However, creating a strong joint between metal and polymers for making a functional partially removable screw is not yet achievable by the current technological advances [8, 9]. Fortunately, the emergence of new classes of biodegradable metals provides an ideal alternative. Three classes of metals have been increasingly studied as biodegradable metals: magnesium, iron and zinc and their alloys [7, 10]. Their potential applications for orthopaedic implants have been extensively studied [11, 12]. After the recent successful clinical trials [13, 14], bone screws made of magnesium alloys are now commercially available for clinical use. In our previous work, we demonstrated that among the three classes of biodegradable metals, pure iron was successfully joined with SS316L by using a friction welding (FW) technique [15]. Thanks to the use of an optimum welding parameter, the welded metals possessed a good combination of strength and ductility and a gradual increase of corrosion rate from stainless steel side to pure iron side. It also showed no toxic effect on normal human osteoblast cells. In practical use of bone screws, the

mechanical properties such as tensile, bending and torsional strengths are important qualities to ensure a successful installation and removal of the screws [16, 17]. Their success also depends on other factors such as the screw diameter and design, the preparation of the hole and the bone mineral density [18, 19]. In the case of a partially removable bone screw, considering the two welded dissimilar metals, special attention should be paid to the weld joint. Therefore, in the present work, we further studied the mechanical and corrosion properties of the pin and screw prototypes out of friction welded pure iron and SS316L. The pin and screw prototypes were subjected to various mechanical and corrosion tests. Also, in vivo study in rats was conducted to evaluate the suitability of the implants for orthopaedic applications.

EXPERIMENTAL SECTION

Friction welding and fabrication of screw prototype

Rods of annealed SS316L and drawn tempered pure iron (both with 9.5 mm diameter and 70 mm length, Goodfellow, UK) were used as base metals for FW and fabrication of the pin and bone screws. Chemical composition and mechanical properties of the rods are presented in Table 1. The surface of the rods has a roughness of 0.34±0.05 μm for SS316L and 0.62±0.06 μm for iron, measured by using a 3D digital microscope (Hirox KH-8700, Japan). By referring to our previous work [15], the FW was done on a modified lathe (Knuht DM 1000A-5.7 kW, Germany) using the following parameters: rotation spindle of 1600 rpm; forging pressure of 33.2 kPa; friction time of 25 s and long burn-off of 15 mm. All specimens were cut from the friction welded iron-SS316L rods with specific dimension according to the requirement for the various tests described in the following.

Table 1 Chemical composition and mechanical properties of the base metals

Metal	Chemical composition (wt%)									Mechanical properties		
	Fe	C	Mn	Si	P	S	Cr	Ni	Mo	UTS (MPa)	YS (MPa)	ε (%)
SS316L	Bal.	0.03	2.3	0.6	-	-	17.8	10.5	2.7	718	637	45
Iron	Bal.	0.002	0.009	0.003	-	-	-	-	-	702	582	9

UTS = ultimate tensile strength; YS = yield strength; and ε = maximum elongation.

Following the design shown in Fig. 1, the bone screw prototypes were machined using a numerical controlled machine. All processes and testing of bone screws were done according to the ASTM F543 standard and a product catalog of T-Bone Screws and Plates (Orthomed Inc., USA) [20]. Dimensional measurement of the screws was conducted by using Image-J NIH software (ImageJ® NIH, USA) and the results is presented in Table 2.

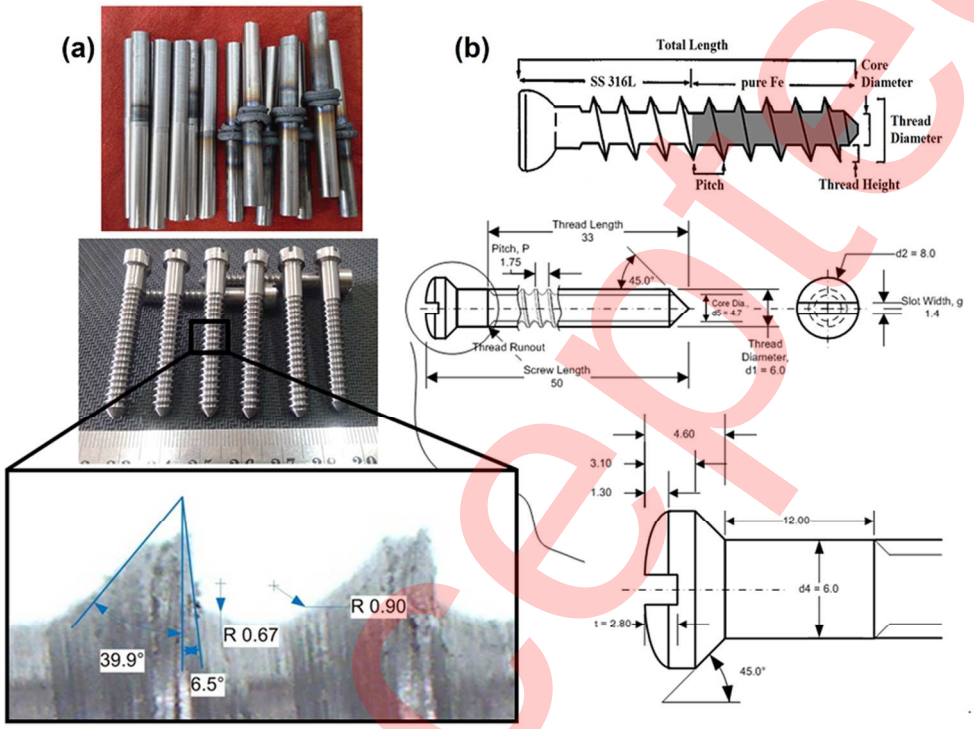

Figure 1 (a) Friction-welded rods and machined screw prototypes, (b) schematic design of the cortical bone screws.

Table 2 Dimension of the bone screw prototype

Dimensional parameter	Value	Dimensional parameter	Value
Screw length (mm)	50	Slot width, g (mm)	1.4
Thread length (mm)	33	t (mm)	2.8
Thread diameter, d1 (mm)	6±0.6	Screw tip (°)	45
Head diameter, d2 (mm)	8	Leading edge radius, r4	0.9±0.1
Shaft diameter, d4 (mm)	6±0.6	Trailing edge radius, r5	0.5±0.1
Core diameter, d5 (mm)	4.7±0.6	Leading edge angle, α (°)	41.2±1.9
Thread pitch, P (mm)	1.75	Trailing edge angle, β (°)	7.4±2.3

Mechanical and corrosion testing

Three modes of mechanical tests were performed: tensile, three-point bending and torsion. The tensile test was done in accordance with the ASTM E8 standard using a universal testing machine (Controlab-TN 20 MD, France) at a loading rate of 1.5 kN/min. Specimens for the tensile test (45 mm length, 6±0.1 mm diameter, 24±0.1 mm gauge length, and 6 mm fillet radius) were cut by a low speed precision sectioning machine (TechCut 5™, Canada) and polished by an abrasive paper grit #800. The three-point bending test was done on rectangular specimens (2.8 x 5 x 16 mm^3) cut by an electrical discharge machine (Sodick AM3L EDM sinkers, USA). The three-point bending data were collected in accordance with the ASTM E290 standard using an axial-torsion fatigue testing system (Instron 8874, USA). The weld joint was loaded until the specimen bent into "U" shape. The bending strength was calculated using equation: $\sigma = 3PC/2wt^2$, where P is the force (N), C is the distance between lower supports (mm) ($C = 2r + 3t \pm t/2$), w is the specimen width and t is the specimen thickness (mm). Finally, the modulus of elasticity (E) was determined using equation: $E = mC^3/4wt^3$, where m is the slop of initial linear elastic portion of load-deflection curve. The torsion test was done in accordance with the ASTM F1264 standard on specimens having dimension of 5 mm diameter and 50 mm length using a manual machine due to limitation of the axial-torsion fatigue testing system in recognizing a torsional angle of less than 140°. Initially, the position of an unloaded specimen was fixed with a balancing water scale by placing an air bubble in the middle of the specimen. At this point, the torsion machine disc and the counter were classified as null. The disc was turned and the angle was recorded in relation with the corresponding force. This step was repeated with other angles and the resulting forces were recorded.

As shown in Fig. 2a, pull-out test was performed using a section of a commonly fresh frozen two years old cow tibia, which was selected to mimic the mechanical strength of the human bone [21, 22]. The cortical bone screw prototype was inserted manually with a screwdriver then extracted by a universal testing machine (Instron Fast Track 8874, USA) with displacement control at a fixed rate of 0.4 mm/min. The force was detected by a 25 kN load cell calibrated to be accurate within ±0.5% of the indicated force. The tests were repeated three times and all procedures were controlled under the provision of the ASTM F543 standard. Finally, the maximum tensile load

(N) at a point when the screws were released from the cow bone was recorded to identify the pull-out strength.

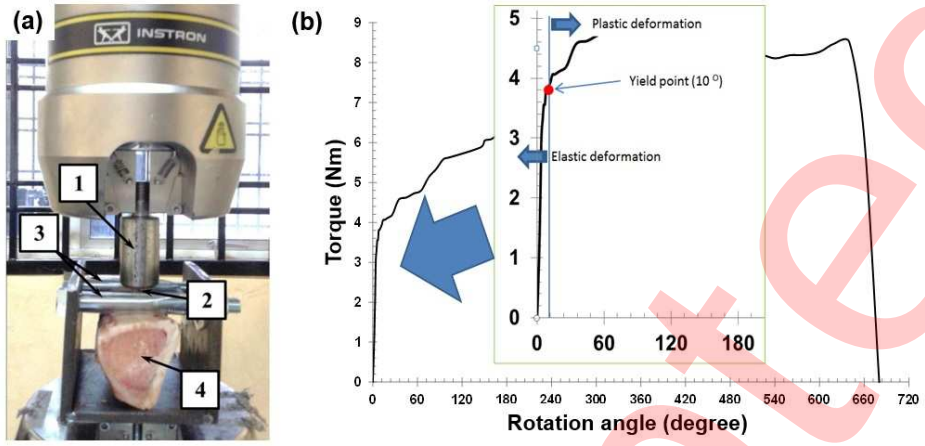

Figure 2 (a) Experimental set-up for uniaxial pull-out test, (b) typical torsion test graph used for determining elastic and plastic deformation limit. Note: (1) pull-out jig, (2) screw prototype, (3) grip span and (4) cow's tibia.

Corrosion tests were carried out by two methods: simple immersion and immersion under torsion. Both methods used a simulated body fluid (SBF) solution prepared based on the work of Kokubo and Takadama [23] with the following composition: 7.996 g NaCl, 0.350 g $NaHCO_3$, 0.224 g KCl, 0.228 g $K_2HPO_43H_2O$, 0.305 g $MgCl_26H_2O$, 40 cm^3 HCl (1 $kmol/m^3$), 0.278 g $CaCl_2$, 0.071 g Na_2SO_4, 6.057 g $NH_2C(CH_2OH)_3$. For the simple immersion, specimens (3 mm diameter and 31 mm length) were immersed in 40 mL SBF at 37±1°C following the ASTM G31 standard for 1, 5, 25 and 60 days with five replications. The SBF solution was refreshed every 24 h and the weight loss of specimens after cleaning was measured. Corrosion rate was calculated by using equation: $CR = \frac{m}{S.t}$ [24], where CR is the corrosion rate (g/cm^2.day), m is the weight loss (g), S is the surface area of the specimen and t is the time (day). Changes in surface morphology were also observed under a stereo optical microscope (Motic Images Plus 2.0, China). Samples of 20 mL was collected from the immersion test solution and were subjected to ion concentration measurement using an atomic absorption spectrophotometer (AAS, AA-7000 Shimadzu, Japan). The corrosion products formed on the specimens after 60 days of immersion were analyzed using an X-ray diffractometer (XRD, Bruker D5000, Siemens, USA) at a scanning rate of 0.05°/min

and a scanning range between 20° and 90°. The immersion test under torsion was performed in 300 mL SBF at 37±1°C by means of a potentiostat (Versastat 3, Princeton Applied Research, USA) using a standard three-electrode configuration and a homemade torsional jig. Graphite served as the counter electrode, Ag/AgCl (KCl 3.5 M) as the reference electrode and specimens under torsion (8.5 cm^2 exposed surface area) as the working electrode. The potentiodynamic polarization test was run at a scanning rate of 0.17 mV/s after a stable open-circuit potential was reached at 1800 s. The corrosion current (i_{corr}) and the corrosion potential (E_{corr}) were determined using Tafel extrapolation method and the corrosion rate was calculated using the equation: $CR = 3.27 * 10^{-3} \frac{i_{corr} EW}{\rho}$, where EW is equivalent weight and ρ is density of the metal, in accordance with the ASTM G102 standard. The torsion load was adapted from the results of torsion test by setting the load limit of elastic and plastic deformations as shown in Fig. 2b.

In vivo study

The study was conducted after obtaining the ethical clearance from the Animal Ethics Committee, Bogor Agricultural University, Indonesia: 024/KEH/SKE/III/2015. Ten male rats (8 weeks, 180-190 g) were used as the animal model. Implant specimens (9 x 1.4 x 0.8 mm^3) were cut from the welded metals. The length of the implant includes three critical sections: iron section, iron-SS316L interface and SS316L section, as determined in our previous study [15]. The rats were subjected to a standard surgical procedure (acclimatization, implantation, monitoring, data collection and termination) under the supervision of the Animal Hospital of Bogor Agricultural University. They were given worm medicine (Praziquantel, 1 mg/kg weight) on day 1 and day 6, antibiotics (Amoxicillin, 20 mg/kg weight) on day 2 to day 5, and anti-protozoa (Metronidazole, 20 mg/kg weight) until day 12 before the implantation phase. Environmental condition was controlled at 25-28°C with 60-80% humidity. Before surgery, the rats were introduced with general anesthetic by injecting ketamine (50 mg/kg weight) and xylazine (5 mg/kg weight) into the intramuscular route of the rat for every hour. The implants were then implanted into the rat femurs with a slit of 9 mm length and 2 mm width (Fig. 3a). Five implants were implanted in each rat bone and fixed by sewing the surrounding muscles using an absorbable 5/0 Vicryl thread. The stitches were then closed with micropore patch. The rats were given antibiotics (Gentamicin, 1 mL/50 kg weight, 0.1 mL/rat tail) every two days for a total of five days. The control group was assigned for post-operative radiographic examination to

visualize the correct placement of implants using a diagnostic X-ray unit (VR-1020 HF Madison, USA). The rats were introduced to ketamine (50 mg/kg weight) and xilazin (5 mg/kg weight) before the imaging process for the anesthetic purpose. Further radiographs were taken as weekly follow-up (day 1, 7, 14, 30 and 60) to identify the morphological changes at the implantation site, such as bone formation. During the observation period, the rats underwent daily physical examination to specifically monitor the wound healing and the tissue growth at the implantation area.

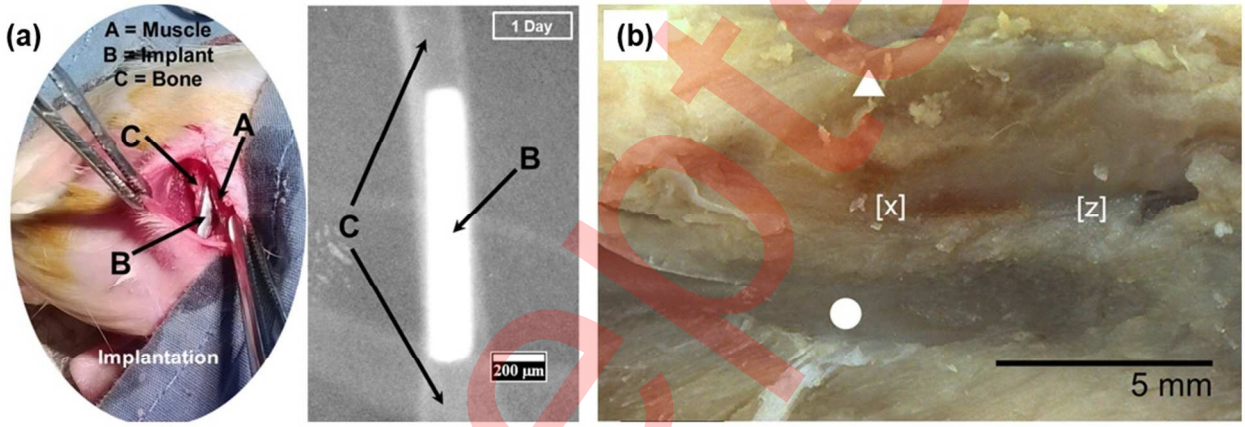

Figure 3 (a) Photograph and radiograph of implant placement in rat's femur, and (b) dried biopsy containing the implant in the right femur. Note: triangle = humeral muscle, circle = humerus bone, [x] iron side of the implant, [z] SS316L side of the implant.

Blood samples of 0.5 mL were withdrawn from the rat venous before the implantation and on day 14, 30 and 60 post-implantation to monitor the systemic response. The concentration of Fe, Ca and P ions in the blood plasma was determined using the AAS. For the purpose of retrieved implant observation, the rats were euthanized by injecting 25 mg sodium thiopental at 60 day post-implantation. A splitting cutting technique was used in lateral direction to remove the implant. The implant was then fixed in neutral buffered 2% formalin solution and the femoral bone was also collected and dried in an oven at 40°C for two days (Fig. 3b) for further analyses by scanning electron microscopy-energy dispersive X-ray spectroscopy (SEM/EDS, TM3000 Hitachi, Japan). After exsanguination, the rat was then incised at implantation site to recover tissue samples (bone and muscle) for further pathological and histological evaluation. The remnant implant was explanted from the tissue, dried and stored in desiccated tube for further

visual and chemical analysis. The tissue was fixed in buffered neutral 10% formaldehyde for further pathological anatomy observation using a stereo optical microscope (Motic Images Plus 2.0, China). The fixed tissue sample was decalcified in 5% nitric acid for 7 days, dehydrated stepwise through ascending series of alcohol solution and finally was degreased in xylene. The tissue was then embedded in paraffin block, sliced at 5 μm by microtome, and stained using hematoxylin and eosin (HE) stains. Cell response at the peri-implant tissue was observed under a CX31 optical microscope (Olympus, Japan) with digital image camera (XCAM1080PHA, China) to capture histological images at the metal interface.

RESULTS AND DISCUSSIONS

Table 3 shows mechanical properties of the friction-welded specimens. Comparing these properties to those of the base metals (Table 1), it is observed that the tensile strength of the weld joint is 5-7% lower than that of iron and SS316L. Also, its elongation is ~70% lower and ~40% higher than that of the SS316L and the iron, respectively. Data from three-point bending test shows that the specimens achieved an ultimate strength of ~1700 MPa, a yield strength of ~650 MPa and a modulus of elasticity of ~18 GPa. The torsion test results shows an ultimate torque of ~8 Nm, an ultimate shear stress of ~0.34 MPa, a modulus of rigidity of ~0.26 GPa and a maximum angle of rotation of ~630^{o}.

Table 3 Mechanical properties of the friction-welded specimens

	Tensile		Bending			Torsion	
σ_U (MPa)	σ_Y (MPa)	ε (%)	σ_U (MPa)	σ_Y (MPa)	M_T (Nm)	τ_{max} (MPa)	G (GPa)
666±7	546±34	13±1	1706±147	656±96	8.3±0.8	0.34±0.03	0.26±0.02

Tensile: σ_U = ultimate tensile strength, σ_Y = yield strength, ε = maximum elongation; bending: σ_U = ultimate flexure stress, σ_Y = yield flexure stress, torsion: M_T = ultimate torque, τ_{max} = ultimate shear stress, G = modulus of rigidity

In this work, a stable and non-oxidized weld joint was formed. The optimum combination of welding parameters, mainly friction time of 25 s and forging pressure of 16.6 kPa, and the smooth surface of the base metals were considered as the determined factor. Dey et al. [25] have shown that a fine surface of a workpiece resulted in a stronger weld joint. Meshram et al. [26]

and Fukumoto et al. [27] stated that an optimum welding parameter, such as adequate heating and forging pressure, prevents the formation of oxide at the weld interface. The obtained torsional strength of the friction-welded specimens (Table 3) is higher than what is required in the ASTM F1264 standard for an intramedullary pin. The specimens with 3 and 5 mm diameter produced maximum torque of 3.27±0.31 and 8.3±0.78 Nm, and breaking angle of 620±165^{o} and 636±174^{o}, respectively. However, in the ASTM F1264 standard, it is stated that pins with 3.5 and 5 mm diameter are supposed to produce a maximum torque of 2.3 and 5.5 Nm, respectively, and a breaking angle of 180^{o} for the both sizes. In this practical use (in vivo implantation of bone screw), the high torsion, tensile and bending strengths of the weld joint will ensure a successful installation and removal of the screw without failing due to fracture or bending.

Fig. 4 shows that a visible sign of corrosion appeared on the weld joint and the iron section after 25 days of immersion in the SBF. A corrosion layer covered the whole specimen surface but started to peel off as specimens were further immersed in the SBF till 60 days (Figs. 4d-e). The XRD analysis on the corrosion product of a 60 days immersed specimen (Fig. 4f) reveals several peak patterns identified as $Fe^{2+}Fe_2^{2+}(PO_4)_2 8H_2O$, $Fe(OH)_3$, $Mg_3(PO_4)_2$ and $Ca_2P_2O_7$ compounds.

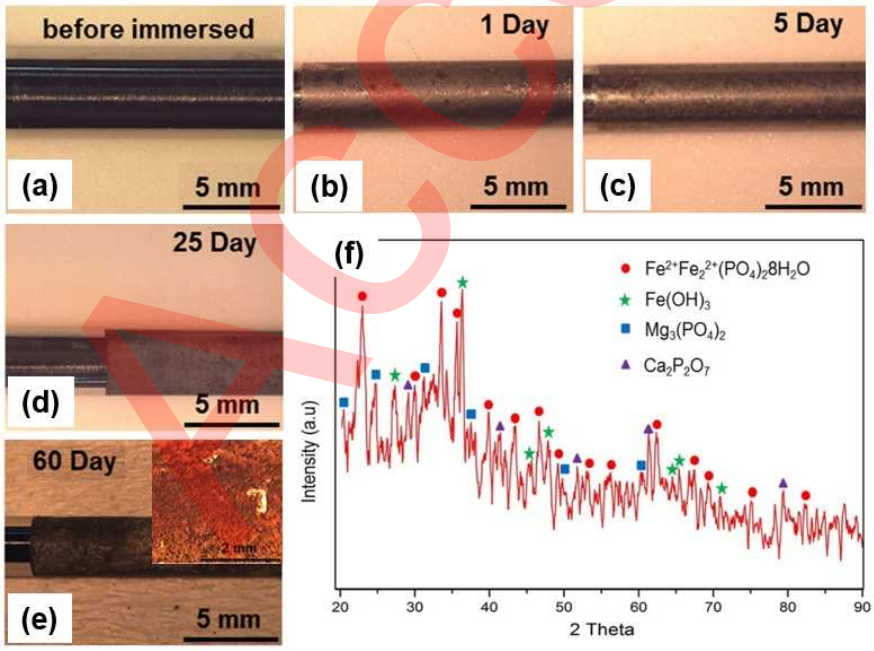

Figure 4 (a-e) Surface appearance of the corrosion specimens, and (f) XRD pattern of corrosion products on the 60 days immersed specimen.

Fig. 5a shows the weight loss curve of the corrosion specimens over time. The weight loss curve is relatively linear with an indication of weight loss increase starting from 25 days to 60 days of immersion. This increase can be associated with the formation of iron hydroxide layer that formed but partially fell off around the day 25. Similar result was observed on pure iron by Zhang et al. [28], where its corrosion rate slowly decreased from day 21 to day 28 of immersion. The average weight loss of the specimens in SBF solution is almost similar to the results obtained by Liu and Zheng [29] for pure iron in Hank's solution which was 16.6 x 10^{-5} g/cm^2.day. This similarity confirms that SS36L section of the specimen did not involve in the corrosion process.

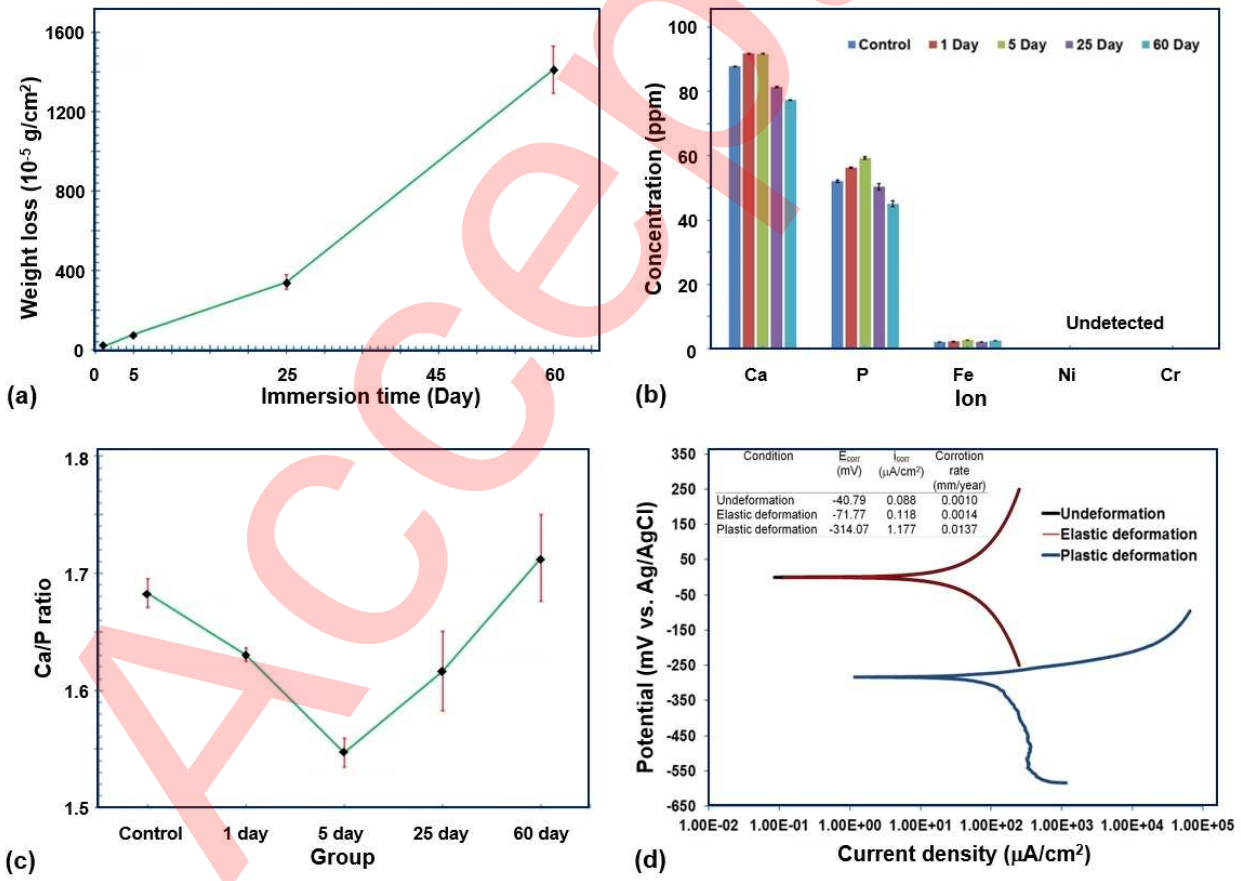

Figure 5 Corrosion behavior of the specimens plotted as: (a) weight loss, (b) concentration of ions released into the test solution, (c) Ca/P ratio of different groups, and (d) polarization curves of specimens under different torsion conditions.

The ion concentration measurement (Fig. 5b) indicates the presence of Ca, P and Fe ions but the absence of Ni and Cr ions. The Ca and P elements come from the SBF solution. Due to some precipitation on the surface of the specimen, the Ca/P ratio decreases from day 1 to day 5, then it gradually increases until day 60 (Fig. 5c). The Ca/P ratio calculation may indicate the ability of the metal surface to form a hydroxyapatite-like layer that attract bone cells [30]. In biodegradable implant applications, it is crucial to determine the amount of released Fe ion to ensure that it maintains the safety level in human body. Zhang et al. [28] proposed a theory that 25% of Fe ion released during 24 h immersion determines a safety level. The average weight loss of the specimen in 40 mL SBF solution was 17.15 x 10^{-5} g/cm^{2}day, so the 25% of the 24 h immersion is 0.0429 mg/mL. Zhu et al. [31] reported that approximately a release of 0.05 mg/mL Fe ion is considered safe for the human body. Therefore, our results suggest that the Fe ion released from the specimen is within the safety level. The average concentration of 2.38 ppm Fe ion is equivalent to 0.0024 mg/mL which is still below the threshold reported by Zhu et al. [31]. The precipitation of Ca and P on the surface of the specimen is commonly observed, as the SBF solution is a rich source of this elements [32].

The results of electrochemical corrosion test on specimens under torsion reveal that there was no noticeable difference in the corrosion potential (E_{corr}) between the deformed and the non-deformed specimens (Fig. 5d). The corrosion current density (i_{corr}) increased from 0.088 μA/cm^2 for the non-deformed specimen to 0.118 μA/cm^2 for the elastically deformed one with similar corrosion resistance value. The corrosion rates for the non-deformed and the elastically deformed specimens are 0.001 mm/year and 0.0014 mm/year, respectively. This indicates elastic deformation by torsion did not affect corrosion behavior of the specimens. Meanwhile, corrosion rate of the plastically deformed specimen is 0.0137 mm/year. This increase of corrosion rate was expected as a common phenomenon related to the stress concentration. Similar finding was reported by Harandi et al. [33] on deformed and cold worked magnesium alloys.

Fig. 6 shows that failure due to pull-out test of the screw occurred at the screw thread-cortical bone interface. The average pull-out force for the 4.7 mm screws was recorded at ~3800 N. Screw design such as thread diameter and pitch plays an important role in increasing pull-out strength of the screw [34]. Wang et al. [35] stated that changing the screw geometry, especially

adjusting the leading edge angle (α) to be less than 30°, increases the pull-out strength to 17%. However, increasing α up to 60° decreases the pull-out strength due to the reduction in "friction resistance" between the screw and the bone. A greater depth of thread and pitch leads to a higher pull-out strength of the screw which is due to greater holding capacity to the bones [36]. While the size of screw peak has no significant effect on the pullout strength [37], the screw length increases the pull-out strength due to higher contact or interface with the bone [38]. Therefore, the bone screw prototype in this work with a full length of 33 mm gives a high pull-out strength.

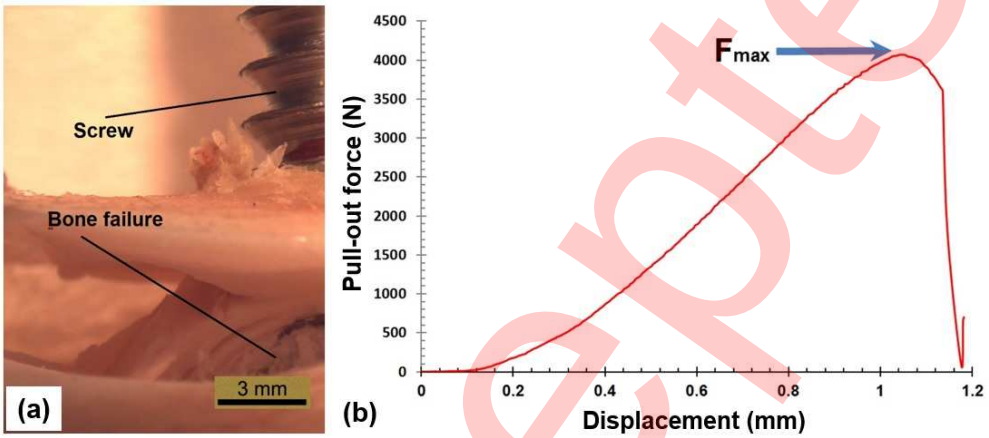

Figure 6 (a) An optical photograph of bone-screw configuration after pull-out test, and (b) a typical pull-out curve showing a load displacement experienced by the screw and the bone.

Additionally, the failure of screw after implantation becomes an important concern in design and manufacturing of bone screws. The calculated shear strength of the screw prototype in this work is 22.2 kN based on Chapman's equation [39]. This value is above the shear strength of the cortical bone suggested by Feerick and McGarry [40]. The maximum pull-out load of the screw prototype of about 3800 N is within the range of the pull-out load of a common cortical screw on composite femur of human cadaver (2600-7800 N) [41]. In the bone healing phase, the strength of bone screw is one of the important factors which supports the stiffness of the bone fixator beside the screw's core diameter and thread [42].

Fig. 7 shows X-ray radiographic images at the implantation site indicating no visual evidence of bleeding, inflammation and gland formation (presence of exudates) around the implants at the 30 day post-implantation. This indicates a successful surgical procedure. Unlike iron-bioceramics

implants that induced tissue formation [43], the iron-SS316L friction welded implant is considerably inert. Inflammation and tissue formation may not be detected by X-ray radiography, so they were investigated through the blood plasma analysis.

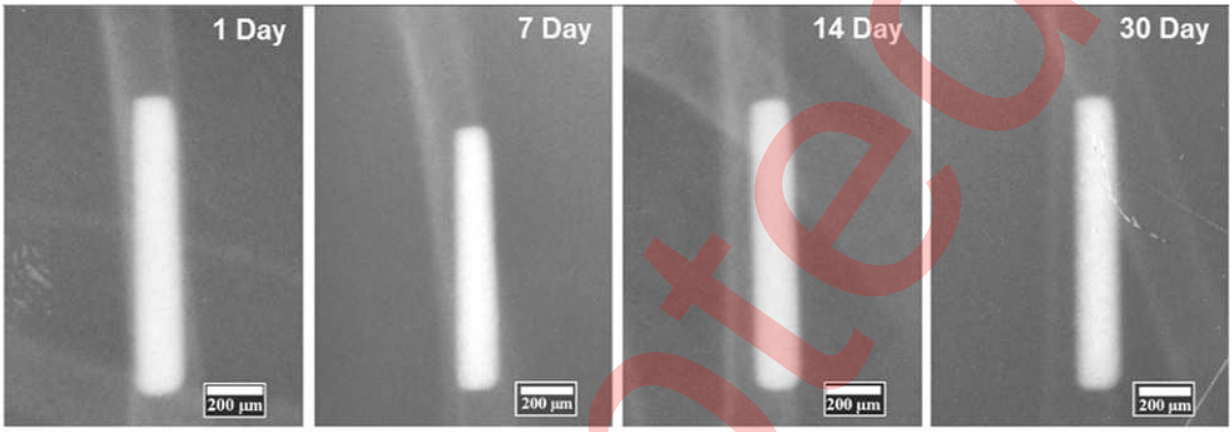

Figure 7 X-ray radiographic images of the implants at 1, 7, 14 and 30 days post-implantation.

Table 4 presents a detailed blood cell analysis showing that red blood cell (RBC), hemoglobin (Hb), hematocrit (PCV), white blood cell (WBC) counts are all in a normal range at all time points. The lowest RBC count was observed on day 14 and the highest RBC count was observed on day 30. The Hb concentration ranges from 14.2 (g/dL) to 16.2 (g/dL), while the PCV count was recorded in between of 38.6% and 47.3%. The neutrophil/lymphocyte ratio changes from 0.3 on day 0 to 0.5 on day 60. The RBC, Hb and PCV counts are in the range of normal category indicating no visible response of toxicity. As part of the immune system, WBC helps the body to fight against various infections. The neutrophils, lymphocytes, eosinophils and monocytes counts are within the range of normal category, indicating no rejection reaction. The neutrophils/lymphocytes ratio of 0.3 to 0.5 is below the normal cellular stress response ratio of 1.5 [44].

Table 4 Blood cell count during implantation period

Cell	Control group				Implant group				P value
	Day 0	Day 14	Day 30	Day 60	Day 0	Day 14	Day 30	Day 60	
RBC (10^6 cells/μL)	8.2 ± 0.6^{ab}	8.5 ± 0.2^{ab}	8.8 ± 1.4^{ab}	7.1 ± 0.6^{a}	8.2 ± 0.6^{ab}	7.6 ± 0.8^{a}	10.8 ± 2.5^{b}	8.8 ± 1.2^{ab}	0.113
Hb (g/dL)	14.2 ± 1.4^{ab}	15.4 ± 0.8^{c}	16.1 ± 1.2^{bc}	13.6 ± 0.3^{a}	14.2 ± 1.4^{ab}	15.2 ± 0.9^{abc}	16.2 ± 1.2^{bc}	14.3 ± 1.1^{ab}	0.053
PCV (%)	38.6 ± 1.2^{a}	42.8 ± 3.2^{cd}	40.3 ± 2.1^{ab}	42.6 ± 1.2^{bc}	38.6 ± 1.2^{a}	41.4 ± 1.2^{ab}	40.8 ± 1.6^{ab}	47.3 ± 2.8^{d}	0
WBC (10^3 cells/μL)	9.7 ± 1.0^{b}	13.3 ± 2.6^{c}	9.1 ± 1.6^{b}	4.9 ± 1.9^{a}	9.7 ± 1.0^{b}	12.9 ± 1.2^{c}	13.5 ± 0.7^{c}	4.9 ± 1.2^{a}	0
Agranulocyte (%WBC)	77 ± 7.5^{a}	68.7 ± 11.6^{a}	65.7 ± 16.6^{a}	68.5 ± 9.2^{a}	77 ± 7.5^{a}	72.7 ± 7.6^{a}	70 ± 3.6^{a}	68 ± 1.7^{a}	0.755
Granulocyte (%WBC)	23 ± 7.5^{a}	31.3 ± 11.6^{a}	34.3 ± 16.6^{a}	31.5 ± 9.2^{a}	23 ± 7.5^{a}	27.3 ± 7.6^{a}	30 ± 3.6^{a}	32 ± 1.7^{a}	0.755
Lymphocyte (%WBC)	73.7 ± 7.8^{a}	65 ± 13.2^{a}	65.7 ± 16.6^{a}	66.5 ± 9.2^{a}	73.7 ± 7.8^{a}	70 ± 8.2^{a}	69.3 ± 4.2^{a}	66 ± 2.0^{a}	0.93
Monocyte (%WBC)	3.3 ± 1.2^{c}	3.7 ± 2.1^{bc}	0^{a}	2 ± 0.0^{bc}	3.3 ± 1.2^{c}	2.7 ± 1.5^{c}	0.7 ± 0.6^{ab}	2 ± 1.0^{bc}	0.008
Basophil (%WBC)	NIL^{a}	NIL^{a}	NIL^{a}	NIL^{a}	NIL^{a}	NIL^{a}	NIL^{a}	NIL^{a}	NIL
Neutrophil (%WBC)	22.7 ± 7.0^{a}	29.7 ± 11.2^{a}	34 ± 16.7^{a}	31 ± 8.5^{a}	22.7 ± 7.0^{a}	26 ± 7.9^{a}	30 ± 3.6^{a}	31.7 ± 1.5^{a}	0.701
Eosinophil (%WBC)	0.3 ± 0.6^{a}	1.7 ± 1.2^{b}	0.3 ± 0.6^{a}	0.5 ± 0.7^{a}	0.3 ± 0.6^{a}	1.3 ± 0.6^{ab}	0^{a}	0.3 ± 0.6^{a}	0.063
Neutrophil/Lymphocyte	0.3 ± 0.1^{a}	0.5 ± 0.2^{a}	0.6 ± 0.4^{a}	0.5 ± 0.2^{a}	0.3 ± 0.1^{a}	0.4 ± 0.2^{a}	0.4 ± 0.1^{a}	0.5 ± 0.0^{a}	0.862

Data shown as mean with standard deviation (x±SD). The same letter in a different row indicates that the difference is not significant ($p > 0.05$).

Table 5 shows concentration of ions released into the blood plasma during the implantation period. The Cr and Ni ions were not detected. The Fe ion concentration decreases from 94 ppm on day 0 to 61 ppm on day 60, while Ca ions increases from 528 ppm to 532 ppm from day 0 to day 60 post-implantation. An increment of Ca/P ratio is identified from 2.9 to 3.3. The Ca/P ratio of 3.3 for the iron-SS316L friction welded implant is close to that of inert SS316L implant (Ca/P ratio of 2.5) [30], which can indirectly confirm no inflammation has occurred. Inflammation usually leads to a reduction of Ca/P ratio due to imbalance of Ca and P minerals during inflammation [45]. Physiological reaction around the implant and its nearby tissues (muscle and bone) changes the ions concentration in blood plasma [46]. At 60 day post-implantation, Fe ion concentration on the implant group (61 ppm) is slightly higher compared to that of the control group (55 ppm) as a result of the corrosion process. The slight increase of Fe ion concentration

could be the reason for the absence of excessive inflammation. This is desirable as in the period of 60 day post-implantation the tissue is still in the recovering and healing phase.

Table 5 Ion concentration in rat's blood plasma

Ion	Concentration (ppm)			
	Control group		Implant group	
	Day 0	Day 60	Day 0	Day 60
Fe	94±1.5	55±4.1	94±1.5	61±2.3
Ca	528±8.2	528±3.4	528±8.2	532±6.4
P	181±1.4	169±4.1	181±1.4	161±3.4
Ca/P	2.9	3.1	2.9	3.3

Fig. 8 shows the distribution of elements on the rat's muscle, the implant and the rat's bone at 60 day post-implantation. Both of the muscle regions (Fig. 8a) in contact with the iron section of the implant [x] and the SS316L section [z] are characterized by the presence of Fe, Ca and P at a similar percentage. On the implant surface (Fig. 8b), the content of P is higher than that on the muscle, while the content of Ca is lower. In the bone area (Fig. 8c), there is an increase of Ca content from ~23 wt% at the iron section [x] to ~35 wt% at weld joint section [y] and to ~40 wt% at SS316L section [z]. A little amount of Ni was detected in [z]. The Ca/P ratio in bone areas of point [x], [y] and [z] is 2.5, 2.4 and 2.7, respectively. Figs. 8d-g show elemental mapping taken on the cross-section of the retrieved rat's muscle and bone at 60 day post-implantation. The muscle region in contact with iron section of implant (Fig. 8d) shows an accumulation of Ca and P elements compared to the region in contact with SS316L section (Fig. 8e) where all elements are distributed evenly. Elemental mapping on the bone's cross-section shows a similar accumulation of Ca and P both at the region in contact with iron section (Fig. 8f) and with SS316L section (Fig. 8g). The implants were retrieved at 60 day post-implantation, a time during which the bone is not fully repaired and remodelled. A metal implant embedded in the body (in vivo) degrades due to electrochemical reaction between the metal and the body fluid [47]. The thickness of corrosion layer contributes to tissue swelling during the wound healing [48]. As shown in the Figs. 8d-g, a thin corrosion layer is present on the surface of the implant at 60 day post-implantation with small distribution of Fe in the local muscle tissue as well as in the bone tissue.

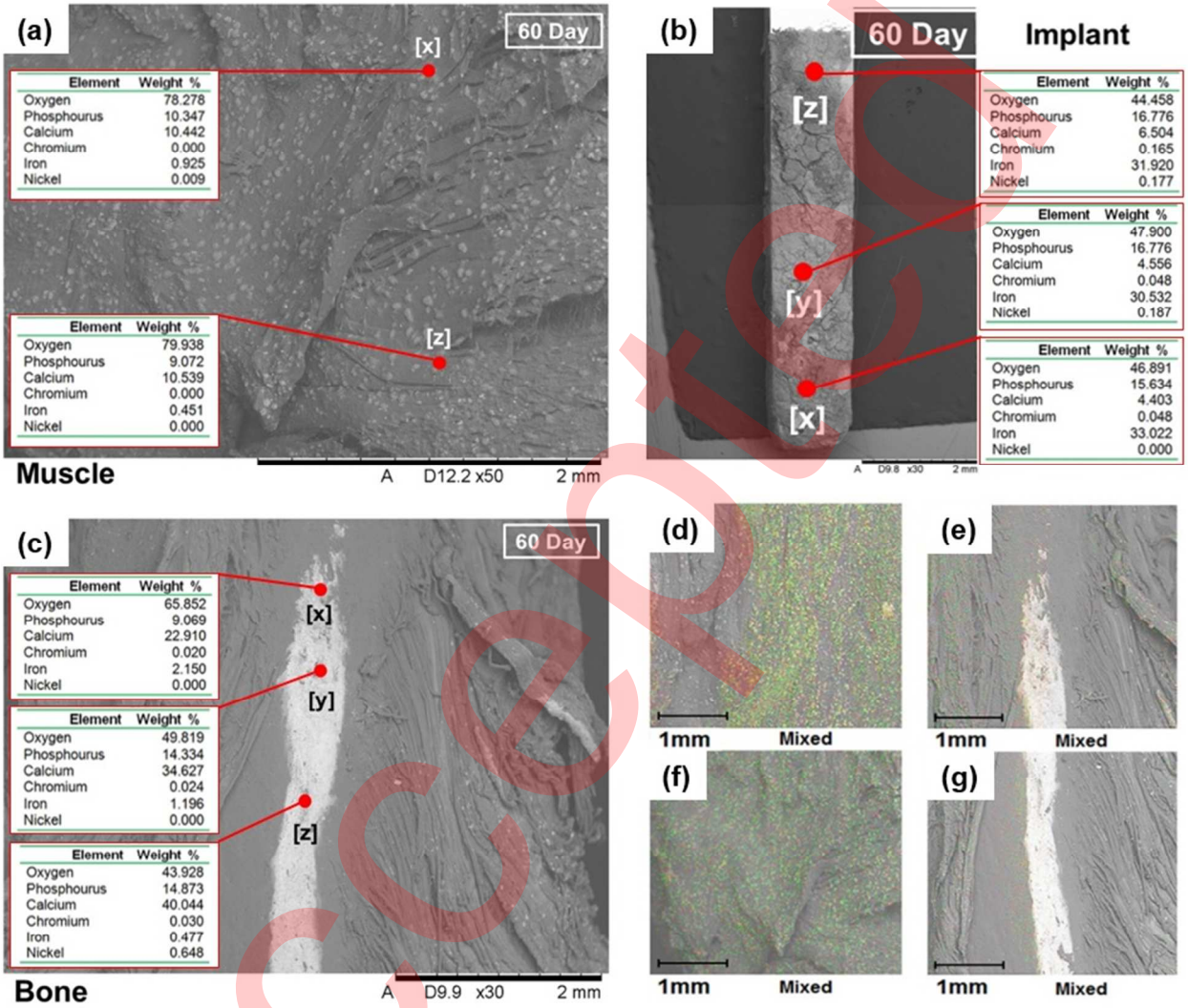

Figure 8 SEM/EDS observation on: (a) the rat's muscle, (b) implant, (c) rat's bone, (d-e) elemental mapping on the cross-section of rat's muscle around [x] and [z], and (f-g) elemental mapping on the cross-section of rat's bone around [x] and [z], all at 60 day post-implantation. Note: [x] pure iron section, [y] weld joint section, and [z] SS316L section.

Figs. 9a-b depict a pathological anatomy of a fixed implantation tissue. It can be seen that the iron section of the implant released corrosion products into the peri-implant tissue marked by the brown color. This is not seen on the tissue in contact with the SS316L section. Figs. 9c-f show histological images of peri-implant tissue at 60 day post-implantation. Corrosion product particles are observed in the surrounding implantation site with a higher accumulation on the

region where there was a contact with the iron section of the implant. A higher number of macrophage cells is also observed at the accumulation site indicating a higher cellular response to the corrosion products. Both corrosion products and macrophage cells are not found in the region which was previously in contact with SS316L section.

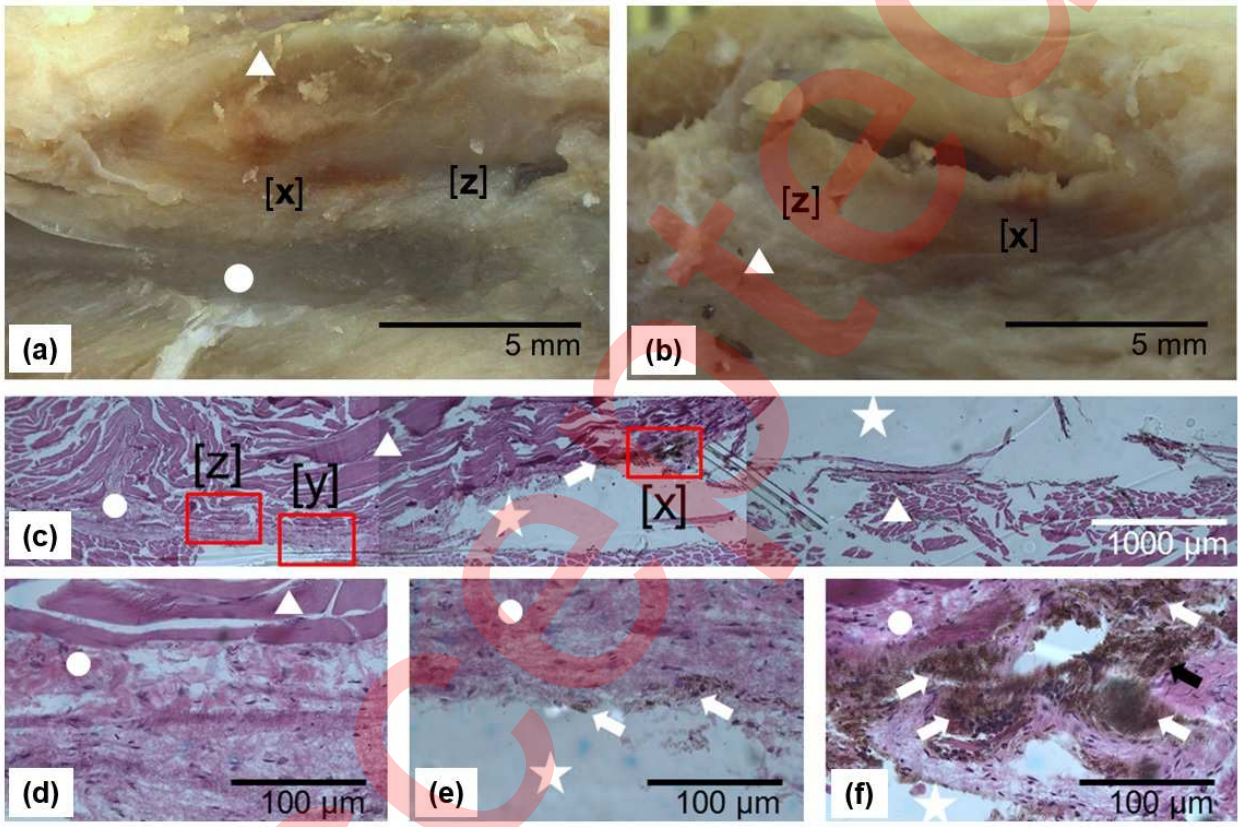

Figure 9 Pathological images of tissue around implant taken at 60 day post-implantation showing (a) sagittal and (b) lateral view; (c) histological images at low magnification, and (d, e, f) high magnification of region in contact with SS316L section [z], weld joint section [y] and iron section [x], respectively. Note: triangle = humeral muscle, circle = humerus bone, star = void (implant region), white arrow = corrosion product, black arrow = macrophages.

The microscopic finding in histological evaluation portrays the accumulation of brown corrosion product particles within the peri-implant site. This has similarity with the result reported in the study of Paramitha et al. [49] where the brown particles from iron-based implants were distributed within the surrounding tissue of implantation site. Ulum et al. [30] reported that a high cellular activity occurred at peri-implant of iron-bioceramic composite implants. These

particles have been the object for macrophage cells to digest as indicated by the significant higher monocyte cell count in the implant group compared to the control group (Table 4). Monocyte cells from the bloodstream transform into macrophages and go into the surrounding implantation site where the corrosion product particles are present [30]. Even though the radiological image analysis is not capable to distinguish the corrosion products, the decreasing radiodensity of the iron section of implant (Fig. 7) is proportional with the pathological anatomy and the histological patterns (Fig. 9). The observed decrease of radiodensity shows a similarity with the radiodensity analysis of iron-bioceramics implants at 70 day post-implantation [43].

CONCLUSIONS

This work demonstrated a successful friction welding technique in joining pure iron and type 316L stainless steel as well as prototyping of partially degradable bone screws. As a result of choosing an optimum welding parameter, the measured values of bending, tensile and torsional strengths were higher than those are suggested in the ASTM F543 standard. Corrosion occurred only on the iron side of the friction welded specimen with an increase on the weight loss rate from day 25 to day 60 of immersion. Nickel or chromium ions were undetected in the corrosion test solution whilst the concentration of iron ion was below the safe threshold value. The corrosion rate of the specimens increased by 10 folds due to plastic deformation induced by torsion. The bone screw prototypes possess a high pull-out strength of 3800 N which is within the range of the pull-out load of a comparable cortical screw on composite femur human cadaver. The detailed blood cell count during implantation of the implants in rats indicated a normal body response without excessive inflammatory reaction. The slight increase of iron ion concentration in rat's blood did not affect the tissue recovering and healing phase. After 60 days of implantation, a thin corrosion layer was formed on the implant surface and elemental Fe was found in the local muscle tissue and in the bone. Histological evaluation on the area of contact with the implant showed a normal presence of macrophage cells at the iron section but an absence of them at the stainless steel section. This work suggests that there is a potential applicability of partially removable bone screw concept made of iron and stainless steel joined by friction welding.

References

1. Hidaka S, Gustilo R. Refracture of bones of the forearm after plate removal. J Bone Joint Surg, 1984, 66: 1241-1243.
2. Bostman O, Pihlajamaki H. Routine implant removal after fracture surgery: A potentially reducible consumer of hospital resources in trauma units. J Trauma Acute Care Surg, 1996, 41: 846-849.
3. Vos DI, Verhofstad MHJ. Indications for implant removal after fracture healing: A review of the literature. Eur J Trauma Emerg Surg, 2013, 39: 327-337.
4. Hallab N, Merritt K, Jacobs JJ. Metal sensitivity in patients with orthopaedic implants. J Bone Joint Surg Am, 2001, 83: 428-436.
5. Brown OL, Dirschl DR, Obremskey WT. Incidence of hardware-related pain and its effect on functional outcomes after open reduction and internal fixation of ankle fractures. J Orthop Trauma, 2001, 15: 271-274.
6. Busam ML, Esther RJ, Obremskey WT. Hardware removal: Indications and expectations. J Am Acad Orthop Sur, 2006, 14: 113-120.
7. Nasution AK, Hermawan H. Degradable biomaterials for temporary medical implants. In Biomaterials and Medical Devices: A Perspective from an Emerging Country. Springer, 2016: 127-160.
8. Kah P, Suoranta R, Martikainen J, *et al.* Techniques for joining dissimilar materials: Metals and polymers. Rev Adv Mater Sci, 2014, 36: 152-164.
9. Amancio-Filho S, Dos Santos J. Joining of polymers and polymer–metal hybrid structures: Recent developments and trends. Polym Eng Sci, 2009, 49: 1461-1476.
10. Zheng YF, Gu XN, Witte F. Biodegradable metals. Mater Sci Eng R, 2014, 77: 1-34.
11. Staiger MP, Pietak AM, Huadmai J, *et al.* Magnesium and its alloys as orthopedic biomaterials: A review. Biomaterials, 2006, 27: 1728-1734.
12. Hort N, Huang Y, Fechner D, *et al.* Magnesium alloys as implant materials – Principles of property design for Mg–RE alloys. Acta Biomater, 2010, 6: 1714-1725.
13. Windhagen H, Radtke K, Weizbauer A, *et al.* Biodegradable magnesium-based screw clinically equivalent to titanium screw in hallux valgus surgery: Short term results of the first prospective, randomized, controlled clinical pilot study. BioMed Eng On, 2013, 12: 62.
14. Lee J-W, Han H-S, Han K-J, *et al.* Long-term clinical study and multiscale analysis of in vivo biodegradation mechanism of Mg alloy. Proc Nat Acad Sci, 2016, 113: 716-721.

15. Nasution AK, Murni NS, Sing NB, *et al.* Partially degradable friction-welded pure iron-stainless steel 316L bone pin. J Biomed Mater Res B, 2015, 103: 31-38.
16. Ivanoff CJ, Sennerby L, Johansson C, *et al.* Influence of implant diameters on the integration of screw implants: An experimental study in rabbits. Int J Oral Maxillofac Surg, 1997, 26: 141-148.
17. Klokkevold PR, Johnson P, Dadgostari S, *et al.* Early endosseous integration enhanced by dual acid etching of titanium: a torque removal study in the rabbit. Clin Oral Impl Res, 2001, 12: 350-357.
18. Yerby S, Scott CC, Evans NJ, *et al.* Effect of Cutting flute design on cortical bone screw insertion torque and pullout strength. J Orthop Trauma, 2001, 15: 216-221.
19. Wilmes B, Drescher D. Impact of bone quality, implant type, and implantation site preparation on insertion torques of mini-implants used for orthodontic anchorage. Int J Oral Maxillofac Surg, 2011, 40: 697-703.
20. OrthoMed. Surgical Instruments Product Catalog. 2013.
21. Taylor D. Scaling effects in the fatigue strength of bones from different animals. J Theor Biol, 2000, 206: 299-306.
22. Topp T, Müller T, Huss S, *et al.* Embalmed and fresh frozen human bones in orthopedic cadaveric studies: which bone is authentic and feasible? A mechanical study. Acta Orthop, 2012, 83: 543-547.
23. Kokubo T, Takadama H. How useful is SBF in predicting in vivo bone bioactivity? Biomaterials, 2006, 27: 2907-2915.
24. Huang T, Cheng J, Zheng Y. In vitro degradation and biocompatibility of Fe–Pd and Fe–Pt composites fabricated by spark plasma sintering. Mater Sci Eng C, 2014, 35: 43-53.
25. Dey HC, Ashfaq M, Bhaduri AK, *et al.* Joining of titanium to 304L stainless steel by friction welding. J Mater Proc Technol, 2009, 209: 5862-5870.
26. Meshram SD, Mohandas T, Reddy GM. Friction welding of dissimilar pure metals. J Mater Proc Technol, 2007, 184: 330-337.
27. Fukumoto S, Katayama K, Okita K, *et al.* Small-scale friction welding of similar and dissimilar stainless steels. Quarterly J Japan Welding Soc, 2009, 27: 99-103.
28. Zhang E, Chen H, Shen F. Biocorrosion properties and blood and cell compatibility of pure iron as a biodegradable biomaterial. J Mater Sci Mater Med, 2010, 21: 2151-2163.

29. Liu B, Zheng YF. Effects of alloying elements (Mn, Co, Al, W, Sn, B, C and S) on biodegradability and in vitro biocompatibility of pure iron. Acta Biomater, 2011, 7: 1407-1420.
30. Ulum MF, Nasution AK, Yusop AH, *et al.* Evidences of in vivo bioactivity of Fe-bioceramic composites for temporary bone implants. J Biomed Mater Res B, 2015, 103: 1354-1365.
31. Zhu S, Huang N, Xu L, *et al*. Biocompatibility of pure iron: In vitro assessment of degradation kinetics and cytotoxicity on endothelial cells. Mater Sci Eng C, 2009, 29: 1589-1592.
32. Witte F, Kaese V, Haferkamp H, *et al.* In vivo corrosion of four magnesium alloys and the associated bone response. Biomaterials, 2005, 26: 3557-3563.
33. Harandi SE, Hasbullah Idris M, Jafari H. Effect of forging process on microstructure, mechanical and corrosion properties of biodegradable Mg–1Ca alloy. Mater Des, 2011, 32: 2596-2603.
34. Michael Hannes Krenn, Wolfgang Peter Piotrowski, Rainer Penzkofer, *et al.* Influence of thread design on pedicle screw fixation. J Neurosurg Spine, 2008, 9: 90-95.
35. Wang Y, Mori R, Ozoe N, *et al.* Proximal half angle of the screw thread is a critical design variable affecting the pull-out strength of cancellous bone screws. Clin Biomech, 2009, 24: 781-785.
36. Ferrara LA, Ryken TC. Screw pullout testing. In An YH, Draughn RA, (Eds). Mechanical testing of bone and the bone-implant interface. Boca raton - Florida: CRC Press 2000.
37. Mehta H, Santos E, Ledonio C, *et al.* Biomechanical analysis of pedicle screw thread differential design in an osteoporotic cadaver model. Clin Biomech, 2012, 27: 234-240.
38. DeCoster TA, Heetderks DB, Downey DJ, *et al.* Optimizing bone screw pullout force. J Orthop Trauma, 1990, 4: 169-174.
39. Patel PSD, Shepherd DET, Hukins DWL. The effect of screw insertion angle and thread type on the pullout strength of bone screws in normal and osteoporotic cancellous bone models. Med Eng Phys, 2010, 32: 822-828.
40. Feerick EM, McGarry JP. Cortical bone failure mechanisms during screw pullout. J Biomech, 2012, 45: 1666-1672.
41. Zdero R, Rose S, Schemitsch EH, *et al.* Cortical screw pullout strength and effective shear stress in synthetic third generation composite femurs. J Biomech Eng, 2006, 129: 289-293.

42. Asnis SE, Ernberg JJ, Bostrom MPG, *et al.* Cancellous bone screw thread design and holding power. J Orthop Trauma, 1996, 10: 462-469.
43. Ulum MF, Arafat A, Noviana D, *et al.* In vitro and in vivo degradation evaluation of novel iron-bioceramic composites for bone implant applications. Mater Sci Eng C, 2014, 36: 336-344.
44. Kannan G, Terrill TH, Kouakou B, *et al.* Transportation of goats: Effects on physiological stress responses and live weight loss. J Animal Sci, 2000, 78: 1450-1457.
45. Conz MB, Granjeiro JM, Soares GA. Hydroxyapatite crystallinity does not affect the repair of critical size bone defects. J Appl Oral Sci, 2011, 19: 337-342.
46. Langton DJ, Sidaginamale RP, Joyce TJ, *et al.* The clinical implications of elevated blood metal ion concentrations in asymptomatic patients with MoM hip resurfacings: A cohort study. BMJ Open, 2012: 001541.
47. Schmutz P, Quach-Vu N-C, Gerber I. Metallic medical implants: Electrochemical characterization of corrosion processes. Electrochem Soc Interf, 2008, 17: 35-40.
48. Carrodeguas RG, De Aza S. α-Tricalcium phosphate: Synthesis, properties and biomedical applications. Acta Biomater, 2011, 7: 3536-3546.
49. Paramitha D, Estuningsih S, Noviana D, *et al.* Distribution of Fe-based degradable materials in mice skeletal muscle. Eur Cell Mater, 2013, S5: 55.

Acknowledgements: This work was supported by the Malaysian Ministry of Higher Education, the Indonesian Ministry of Education and Culture and the Natural Sciences and Engineering Research Council of Canada (NSERC). The authors thank B Panjaitan, D Paramitha, MA Setiadi and IWK Karja for their help during the in vivo animal implantation and histological analysis.

Author contributions: All authors contributed to the preparation and discussion of the manuscript. The final version of the manuscript was approved by all authors.

Conflict of interest: The authors declare that they have no conflict of interest.

Hendra Hermawan received his PhD degree in materials engineering from Laval University in 2009. After spending some academic years in Asia, he returned to Laval University in 2014 as an assistant professor and also a researcher at CHU de Québec Research Center, Québec, Canada. His research interests include biomaterials, biodegradable metals and corrosion.

Ahmad Kafrawi Nasution received his PhD degree in biomedical engineering from University of Technology of Malaysia in 2016 under the supervision of Dr. Hermawan. He is now a lecturer at the Department of Mechanical Engineering, Muhammadiyah University of Riau in Indonesia where he is building a research group on biomaterials.

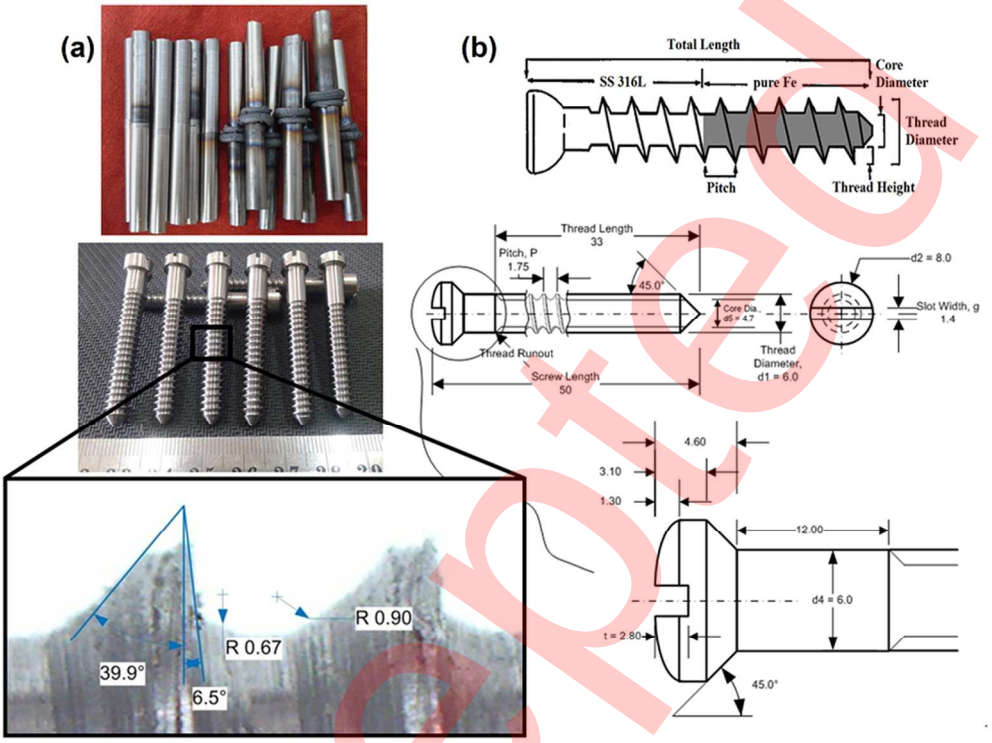

Fig. 1

84x62mm (300 x 300 DPI)

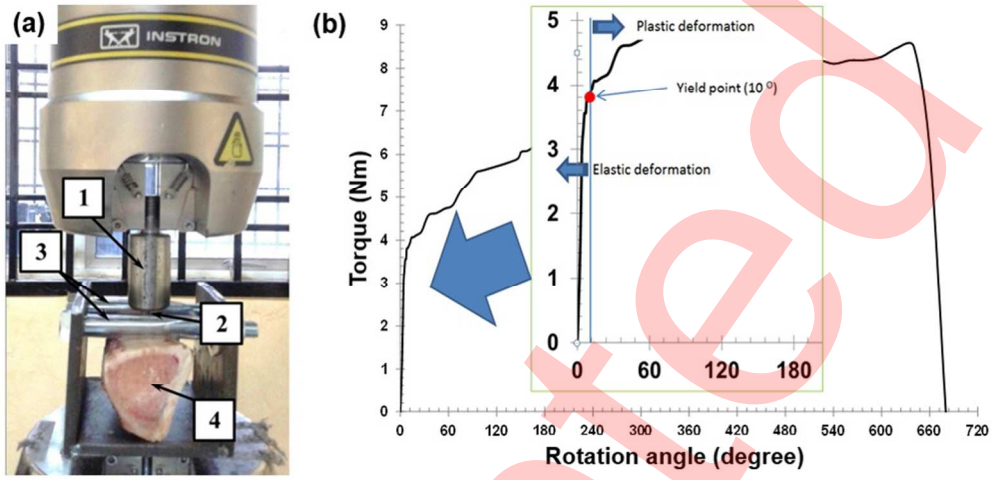

Fig. 2

84x41mm (300 x 300 DPI)

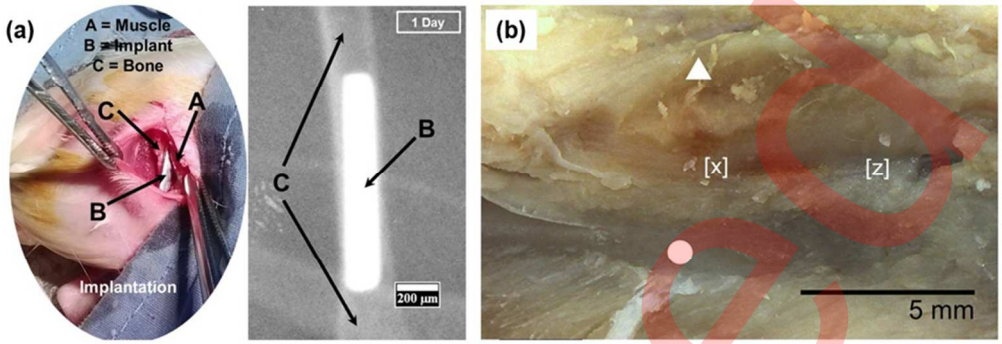

Fig. 3

84x29mm (300 x 300 DPI)

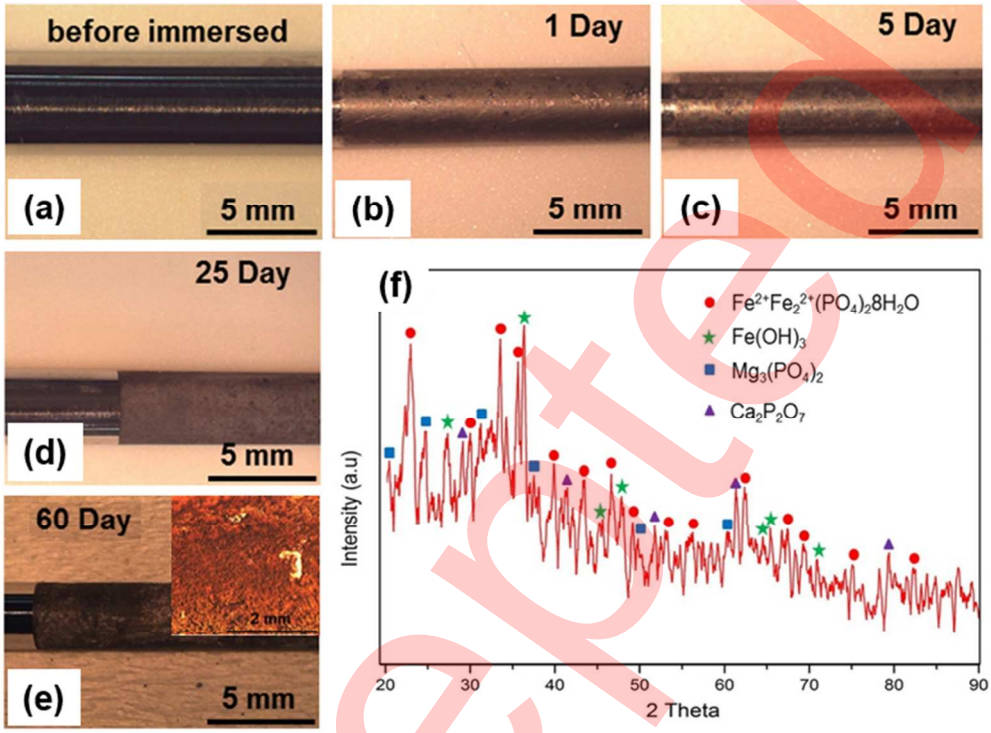

Fig. 4

84x63mm (300 x 300 DPI)

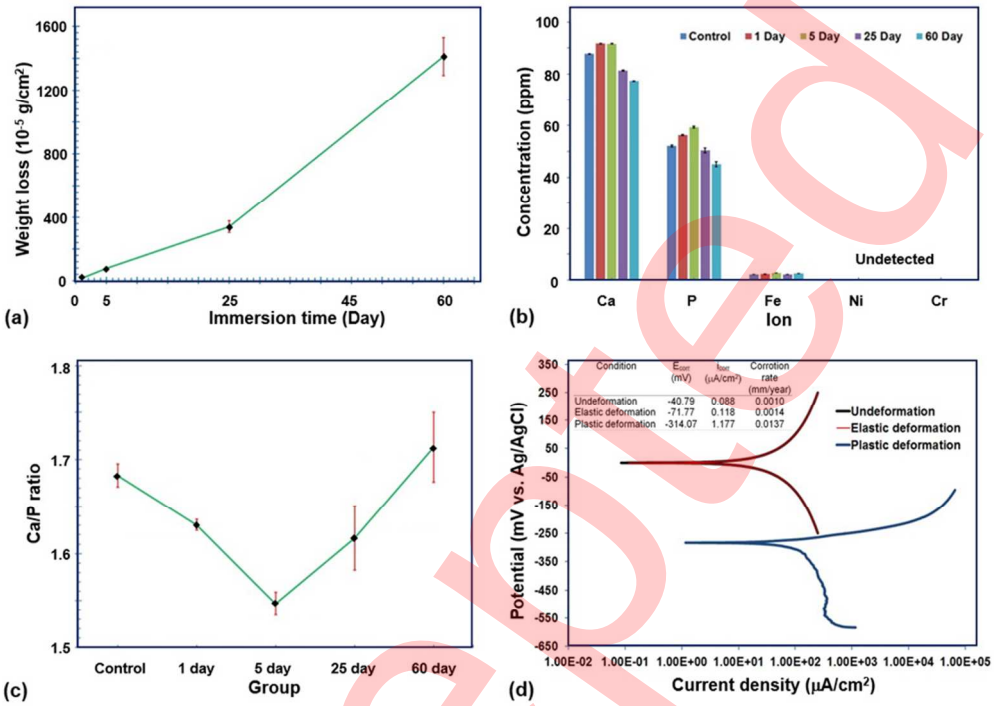

Fig. 5

84x60mm (300 x 300 DPI)

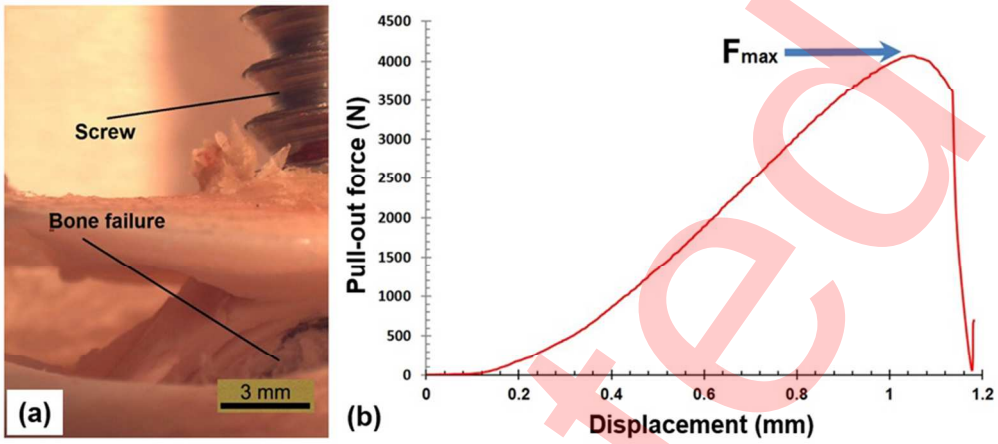

Fig. 6

84x37mm (300 x 300 DPI)

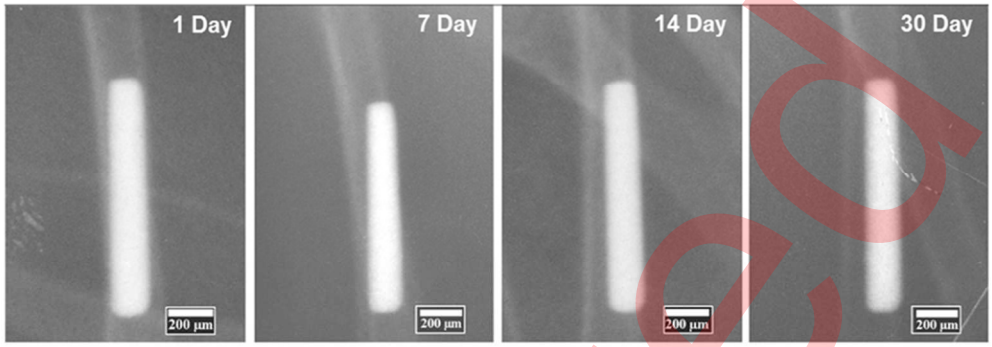

Fig. 7

84x29mm (300 x 300 DPI)

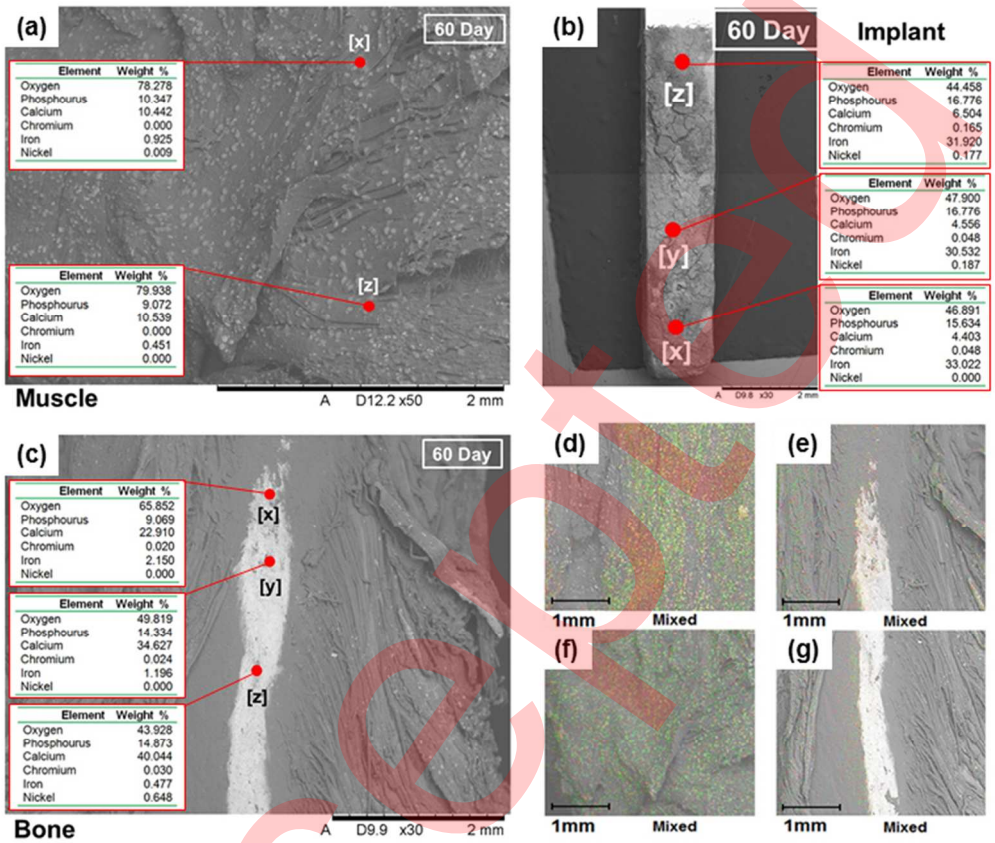

Fig. 8

84x71mm (300 x 300 DPI)

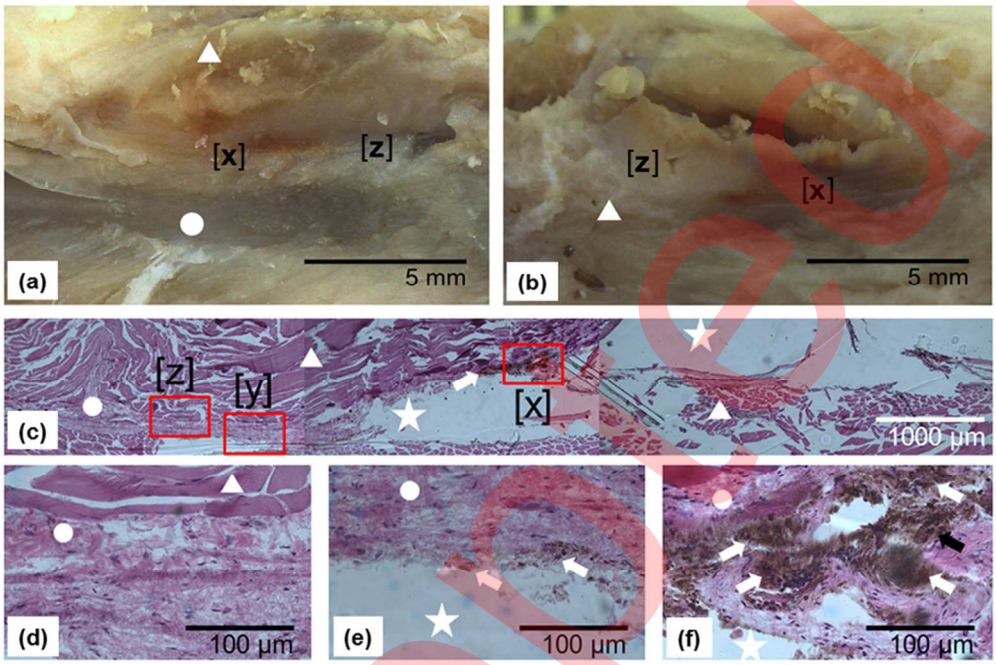

Fig. 9

84x56mm (300 x 300 DPI)